A Luminescent Thermometer Exhibiting Slow Relaxation of the Magnetization: Towards Self-Monitored Building Blocks for Next-Generation Optomagnetic Devices

Dylan Errulat,[a‡] Riccardo Marin,[a,#‡] Diogo A. Gálico,[b,⊥] Katie L. M. Harriman,[a] Amelie Pialat,[a] Bulat Gabidullin,[a] Fernando Iikawa,[c] Odilon D. D. Couto Junior,[c] Jani O. Moilanen,[d] Eva Hemmer,[a*] Fernando A. Sigoli,[b*] and Muralee Murugesu[a*]

[a] *Department of Chemistry and Biomolecular Sciences, University of Ottawa, Ottawa, Ontario K1N 6N5, Canada*

[b] *Institute of Chemistry, University of Campinas, UNICAMP, P.O. Box 6154, Campinas, Sao Paulo 13083-970, Brazil*

[c] *Institute of Physics "Gleb Wataghin", University of Campinas, UNICAMP, P.O. Box 6165, Campinas, Sao Paulo 13083-970, Brazil*

[d] *University of Jyväskylä, Department of Chemistry, Nanoscience Centre, P.O. Box 35, FI-40014, Finland*

Current addresses:

[#] *Fluorescence Imaging Group, Departamento de Física de Materiales, Universidad Autónoma de Madrid, Madrid 28049, Spain*

[⊥] *Department of Chemistry and Biomolecular Sciences, University of Ottawa, Ottawa, Ontario K1N 6N5, Canada*

TABLE OF CONTENT

Summary of crystallographic data

Table S1. Crystallographic data and selected data collection parameters for **1** and **2**.

Compound	**[Dy_2(bpm)(tfaa)$_6$] (1)**	**[Gd_2(bpm)(tfaa)$_6$] (2)**
Empirical formula	$C_{38}H_{30}F_{18}dDy_2N_4O_{12}$	$C_{38}H_{30}F_{18}Gd_2N_4O_{12}$
Formula weight, a.u.	1401.66	1391.16
Crystal size, mm	0.493x0.0427x0.212	0.474x0.254x0.060
Crystal system	Monoclinic	Monoclinic
Space group	$P2_1/n$	$P2_1/n$
Z	2	2
a, Å	12.5776(3)	12.6460(8)
b, Å	13.0731(3)	13.1377(8)
c, Å	16.4365(3)	16.4864(11)
α, °	90	90
β, °	111.4160(10)	111.6130(10)
γ, °	90	90
Volume, $Å^3$	2516.02(10)	2546.5(3)
Calculated density, Mg/m^3	1.850	1.814
Absorption coefficient, mm^{-1}	3.072	2.706
T (K)	200(2)	200(2)
F(000)	1352	1344
Θ range for data collection, °	2.365 to 27.86	1.752 to 27.877
Limiting indices	h = ±16, k = -16, 17, l = ±21	h = ±16, k = ±17, l = ±21
Reflections collected / unique	6013 / 5292	6052 / 4862
R(int)	0.0340	0.0461
Completeness to Θ = X, %	25.242, 100	25.242, 100
Max. and min. transmission	0.7456 and 0.5574	0.7456 and 0.5746
Data / restraints / parameters	6013 / 91 / 374	6052 / 101 / 368
Goodness-of-fit on F^2	1.054	1.017
Final R indices [$I>2\sigma(I)$][a]	R_1 = 0.0199, wR_2 = 0.0457	R_1 = 0.0277, wR_2 = 0.0546
R indices (all data)	R_1 = 0.0251, wR_2 = 0.0483	R_1 = 0.0407, wR_2 = 0.0601
Largest diff. peak/hole, $e \cdot Å^{-3}$	0.467 and -0.0508	0.615 and -0.626

[a] $R = R_1 = \sum||F_0| - |F_c||/ \sum|F_0|$; $wR_2 = \{\sum[w (F_0^2 - F_c^2)^2/\sum[w(F_0)^2]]^{1/2}$; $w = 1/[\delta^2(F_o^2) + (ap)^2 + bp]$, where $p = [\max (F_0^2, 0) + 2F_c^2]/3$

Additional magnetic characterization

Table S2. Lowest calculated Kramers doublets (KD) and their ***g***-tensors for **1** as well as the angle (θ) between the magnetic axes of ground KD and each excited KD.

KD	E / cm^{-1}	g_x	g_y	g_z	θ
1	0.000	0.008	0.026	19.281	-
2	101.468	0.328	0.551	16.339	17.807
3	146.685	1.606	2.011	14.220	35.535
4	190.963	3.969	5.237	7.631	12.271
5	234.814	2.203	3.586	11.785	106.116
6	316.352	0.162	0.211	16.654	99.769
7	384.521	0.012	0.103	17.695	91.424
8	467.066	0.014	0.037	19.159	126.942

Table S3. Percentage composition of the SO-RASSI wave functions for each m_j state of the ground multiplet (J = 15/2) in **1**.

m_j	KD1		KD2		KD3		KD4		KD5		KD6		KD7		KD8	
-15/2	89.8	0.0	1.0	0.0	2.6	0.1	2.1	0.0	0.1	0.2	0.0	0.3	0.6	0.0	0.0	3.2
-13/2	0.4	0.0	68.0	0.6	6.1	1.0	4.6	0.6	1.6	0.4	0.1	0.3	2.3	0.2	0.0	13.9
-11/2	8.4	0.0	12.6	0.0	31.9	0.8	12.8	0.5	2.8	1.8	0.3	0.5	3.0	0.4	0.0	24.2
-9/2	1.0	0.0	11.2	0.3	36.4	0.5	6.2	1.5	9.1	3.3	0.4	3.6	2.3	0.6	0.0	23.5
-7/2	0.1	0.0	2.9	0.1	8.1	0.5	33.4	2.6	1.9	19.5	2.4	9.1	0.9	2.8	0.2	15.6
-5/2	0.3	0.0	1.8	0.1	1.4	0.6	13.9	2.7	22.6	6.9	14.9	17.9	1.6	5.7	0.6	9.2
-3/2	0.1	0.0	0.9	0.1	5.1	1.3	5.2	2.8	9.7	4.7	3.0	35.0	10.3	15.6	1.1	5.1
-1/2	0.0	0.0	0.3	0.2	1.1	2.6	7.3	3.8	1.0	14.4	9.7	2.6	27.6	26.0	1.1	2.2
1/2	0.0	0.0	0.2	0.3	2.6	1.1	3.8	7.3	14.4	1.0	2.6	9.7	26.0	27.6	2.2	1.1
3/2	0.0	0.1	0.1	0.9	1.3	5.1	2.8	5.2	4.7	9.7	35.0	3.0	15.6	10.3	5.1	1.1
5/2	0.0	0.3	0.1	1.8	0.6	1.4	2.7	13.9	6.9	22.6	17.9	14.9	5.7	1.6	9.2	0.6
7/2	0.0	0.1	0.1	2.9	0.5	8.1	2.6	33.4	19.5	1.9	9.1	2.4	2.8	0.9	15.6	0.2
9/2	0.0	1.0	0.3	11.2	0.5	36.4	1.5	6.2	3.3	9.1	3.6	0.4	0.6	2.3	23.5	0.0
11/2	0.0	8.4	0.0	12.6	0.8	31.9	0.5	12.8	1.8	2.8	0.5	0.3	0.4	3.0	24.2	0.0
13/2	0.0	0.4	0.6	68.0	1.0	6.1	0.6	4.6	0.4	1.6	0.3	0.1	0.2	2.3	13.9	0.0
15/2	0.0	89.8	0.0	1.0	0.1	2.6	0.0	2.1	0.2	0.1	0.3	0.0	0.0	0.6	3.2	0.0

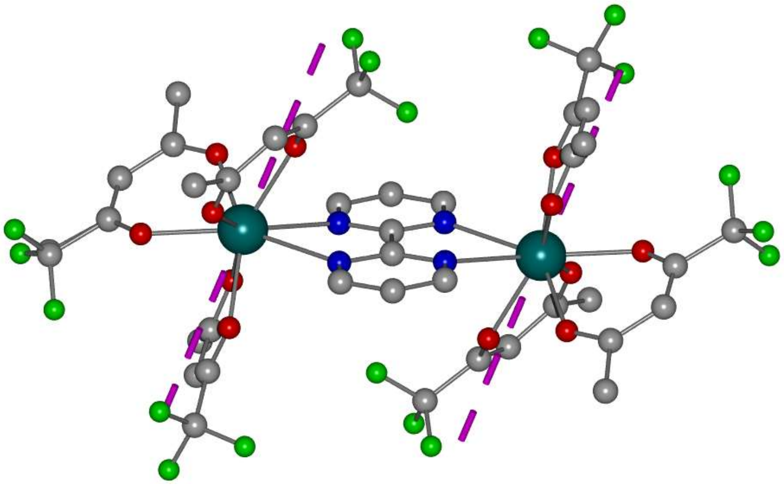

Figure S1. Orientation of the principal magnetic axes of the ground Kramers doublet (dashed magenta lines) for **1**.

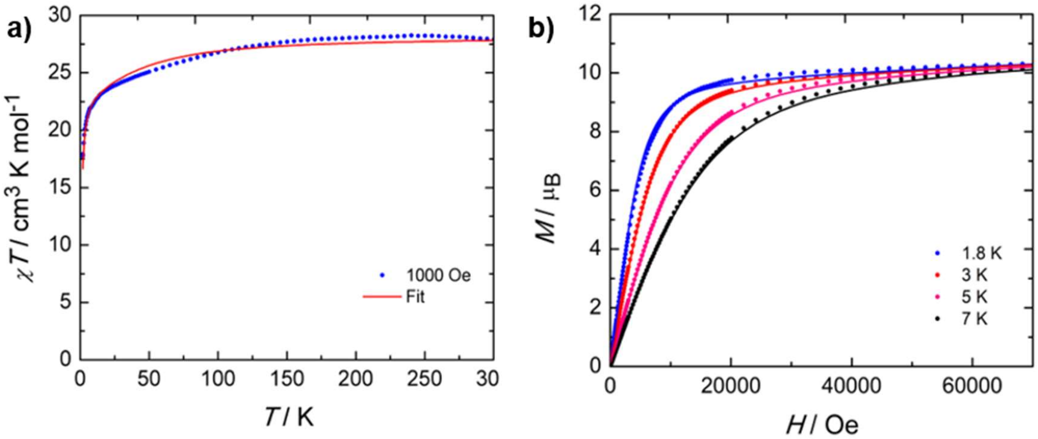

Figure S2. The plot of χT as function of temperature (a) and the plots of the magnetization (M) as function of magnetic field (H) at the indicated temperatures (b). The experimental data of compound **1** are represented by filled circles and the solid lines are the calculated curves. Calculated plots were obtained by using the exchange parameter -0.046 cm^{-1} and include only the ground Kramers doublets of each Dy^{III} center into the exchange interaction.

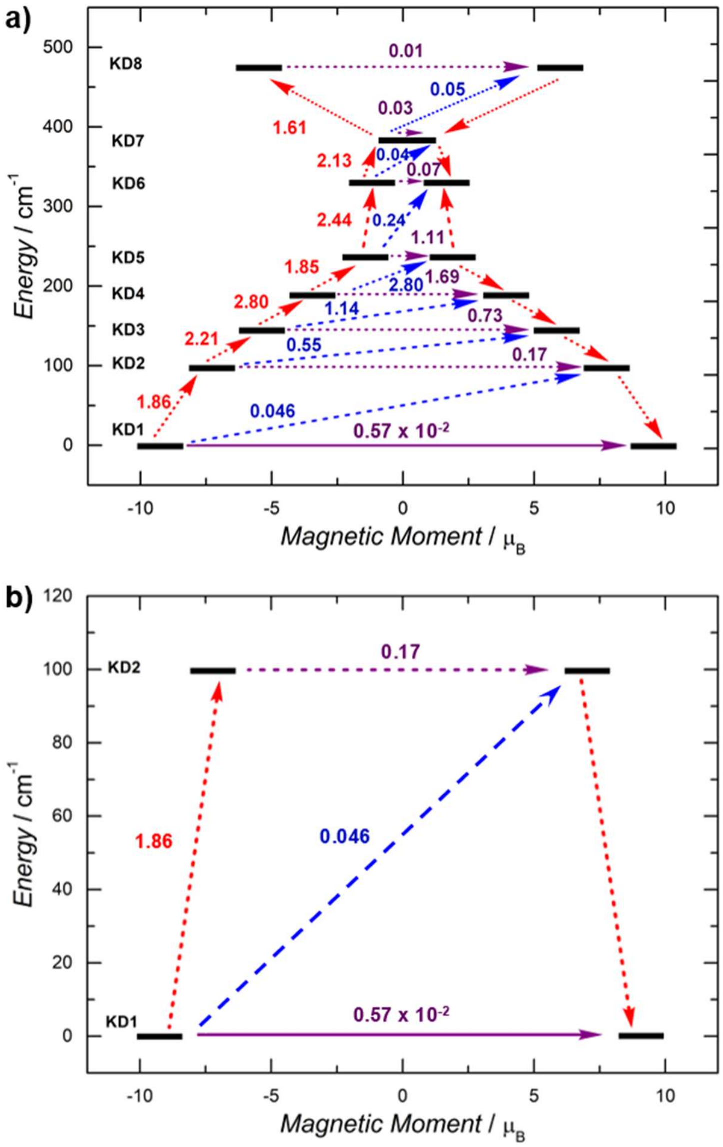

Figure S3. Barrier to spin reversal for **1**. The numbers show the average transition magnetic moment matrix element (transition probabilities) between KD 1-8 (a) and KD 1-2 (b). Red, blue, and purple lines denote the transition probabilities for the direct vertical transitions, Orbach process, and quantum tunneling processes respectively.

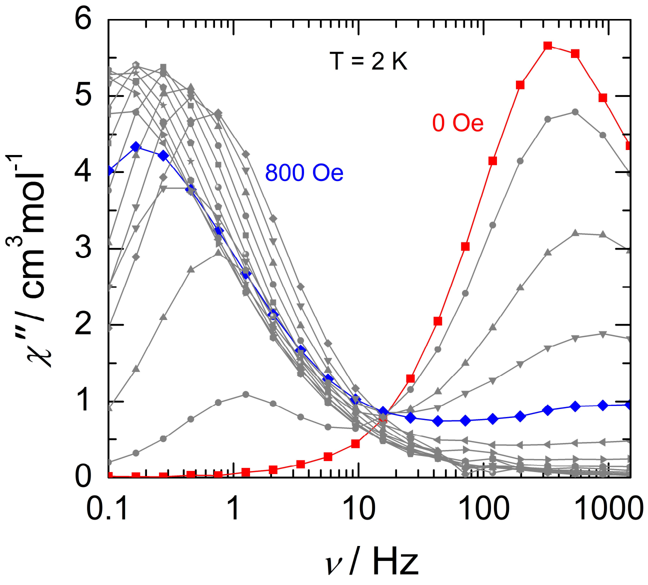

Figure S4. Field dependence of the out-of-phase (χ'') magnetic susceptibility at 2 K in different applied dc fields up to 3000 Oe for a solid-state sample of **1**. 0 Oe (red) and 800 Oe (blue) static field highlighted as frequency-dependent ac susceptibility measurements were completed under these conditions.

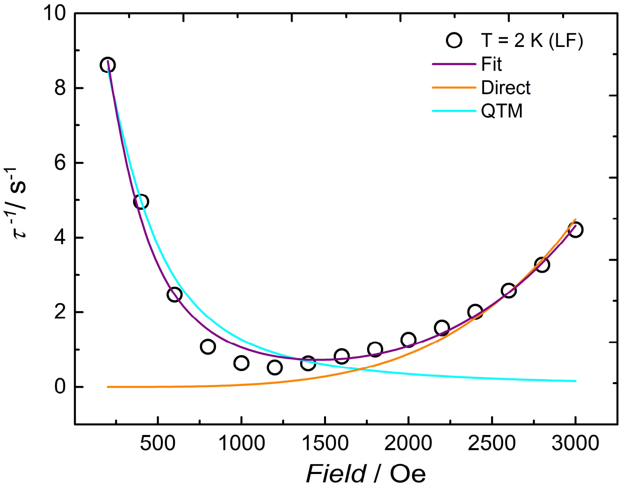

Figure S5. Field dependence of the magnetization relaxation times (τ) of compound **1** in different applied dc fields up to 3000 (200 Oe increments) collected at 2 K in the low frequency regime (LF). The purple line represents the best fit of the experimental data to Eq. 1. The orange and teal lines are the individual components of the relaxation model for the direct and the QTM processes.

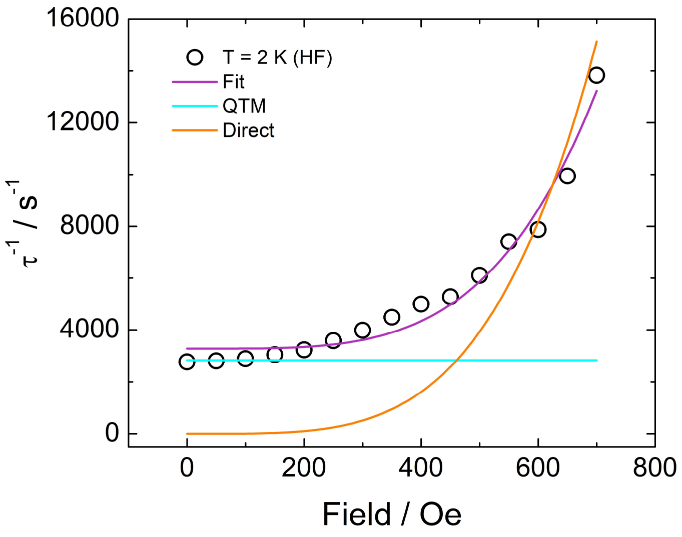

Figure S6. Field dependence of the magnetization relaxation times (τ) of compound **1** in different applied dc fields up to 750 Oe (50 Oe increments) collected at 2 K in the high frequency regime (HF) The purple line represents the best fit of the experimental data to Eq. 1. The orange and teal lines are the individual components of the relaxation model for the direct and the QTM processes.

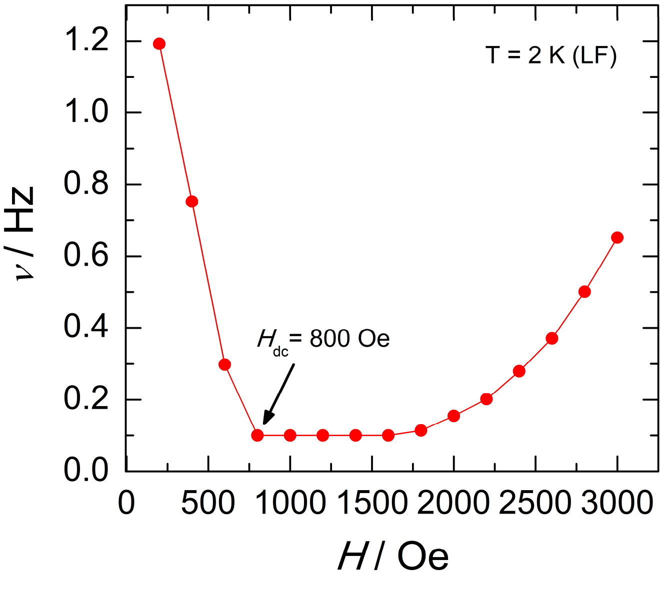

Figure S7. Field dependence of the characteristic low frequency (LF), depicting an optimal static field of 800 Oe at 2 K. The characteristic frequency is obtained from the fit of the field-dependent χ" signal to a Gaussian distribution. The solid line is a guide for the eye.

Table S4. Summary of fit parameters obtained by Eq. 1 of the field dependence of the magnetization relaxation times (τ) of compound **1** for the two peaks located in the low frequency (LF) and high frequency (HF) regions of the studied range collected in 200 and 50 Oe-increments, respectively.

Solid		**0 Oe**	**800 Oe**
Direct	A	2.586 x 10^{-14} s^{-1}Oe^{-4}K^{-1}	2.070 x 10^{-8} s^{-1}Oe^{-4}K^{-1}
QTM	B_1	12.783	3284.32
	B_2	1.164 x 10^{-5}	1.0 x 10^{-12}

Table S5. Summary of fit parameters obtained by Eq. 2, 3 of the temperature dependence of the magnetization relaxation times (τ) provided by the out-of-phase (χ") magnetic susceptibility for solid and solution-state samples of **1**.

Solid		**0 Oe**	**800 Oe**
QTM	τ_{QTM}	3.65 x 10^{-4} s	0.326 s
Raman	C	0.001 s^{-1} K^{-n}	0.010 s^{-1} K^{-n}
	n	6.53	5.35
Orbach	τ_0	-	1.96 x 10^{-5} s
	U_{eff}	-	33.17 K

Solution		**0 Oe**	**800 Oe**
QTM	τ_{QTM}	2.18 x 10^{-2} s	-
Raman	C	3.88 s^{-1} K^{-n}	0.091 s^{-1} K^{-n}
	n	2.39	3.50
Orbach	τ_0	7.37 x 10^{-6} s	1.24 x 10^{-5} s
	U_{eff}	53.32 K	50.74 K

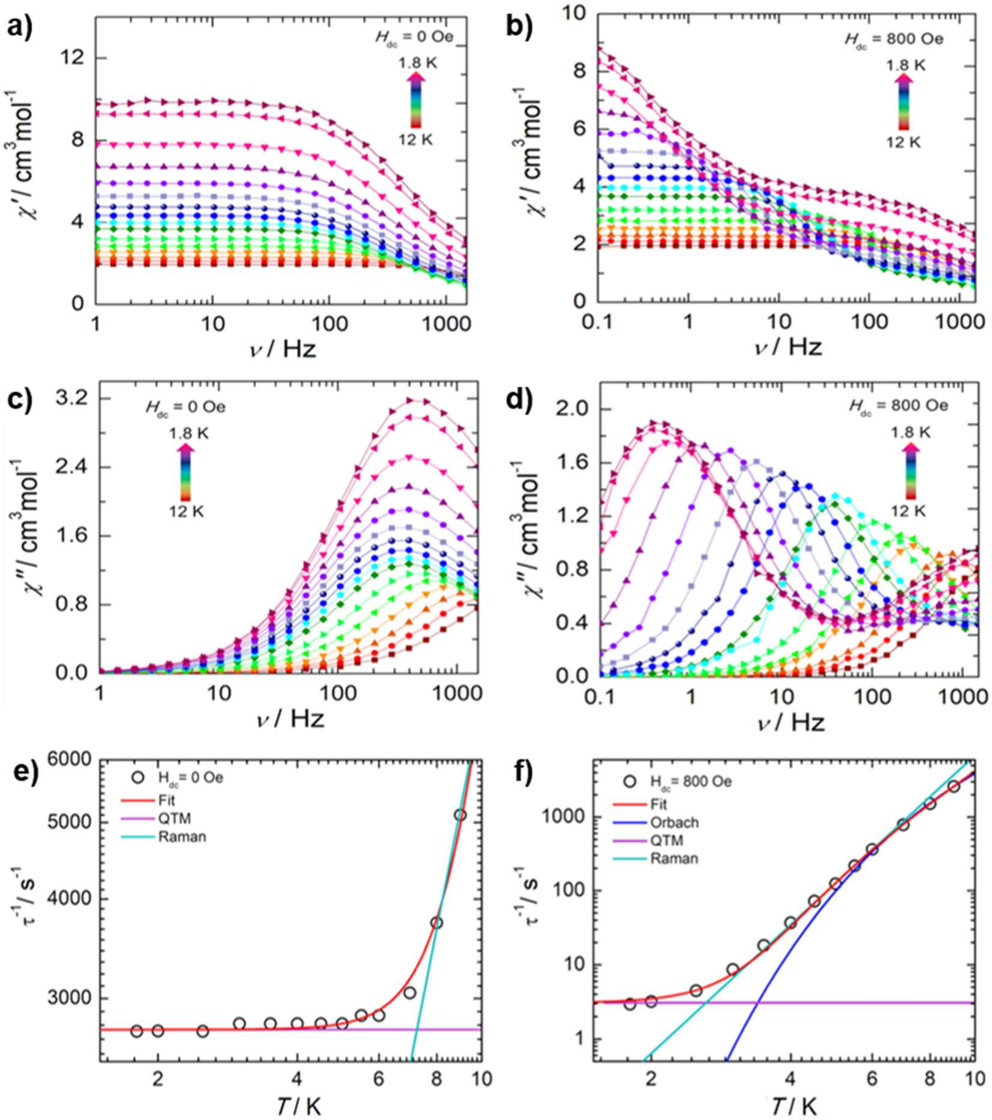

Figure S8. Frequency dependence of the in-phase (χ') out-of-phase (χ'') magnetic susceptibility for solid **1** in the absence (a and c) and under a 800 Oe applied static field (b and d) as a function of temperature. Temperature dependence of the magnetization relaxation times (τ) in the absence of magnetic field (e) and under a 800 Oe applied static field (f). The solid red lines represent the best fit of the data to Eq. 2 or 3. The blue, purple, and teal lines are the individual components of the relaxation model for the Orbach, Raman, and QTM processes.

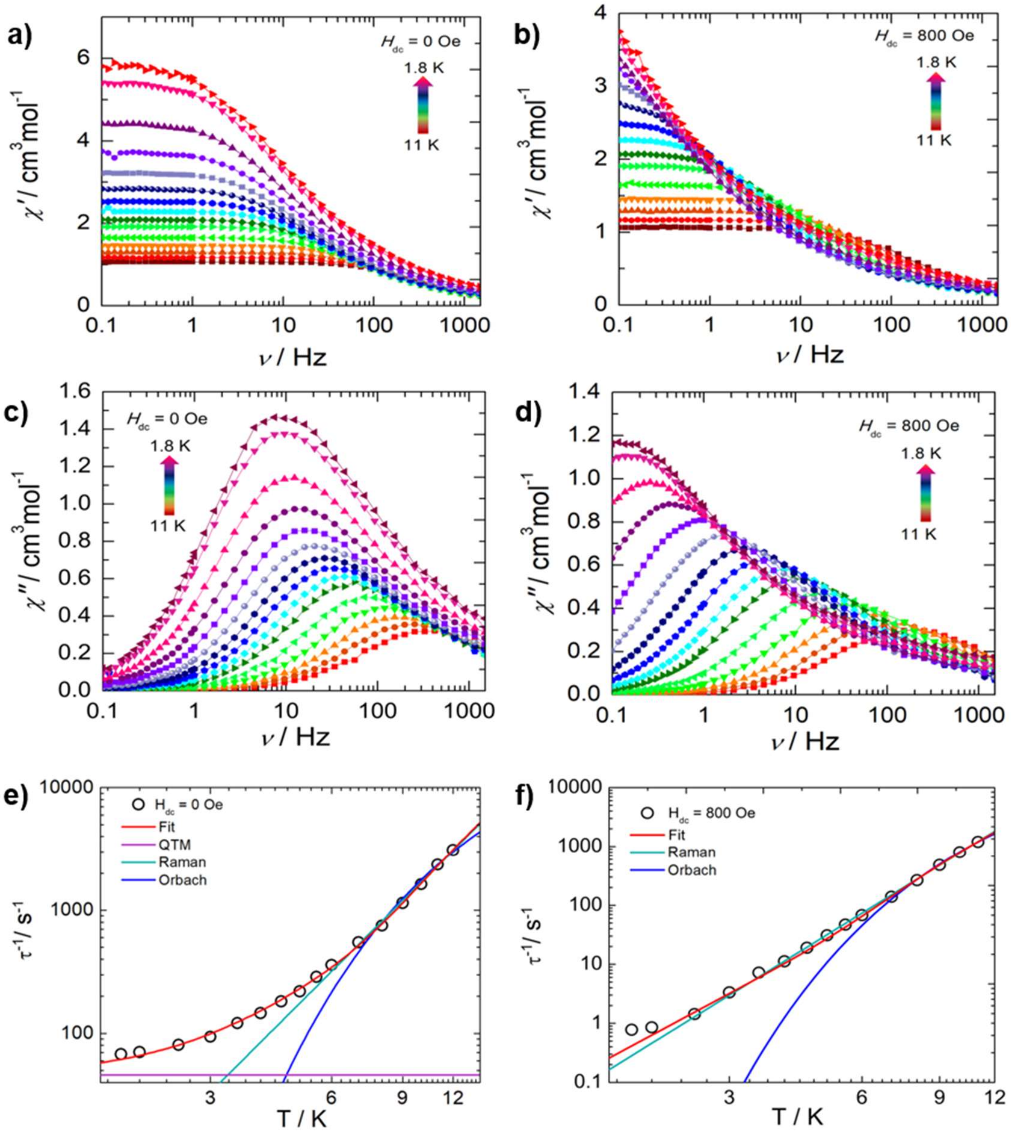

Figure S9. Frequency dependence of the in-phase (χ') and out-of-phase (χ") magnetic susceptibility for a solution sample of **1** in the absence (a and c) and under a 800 Oe applied static field (b and d) as a function of temperature performed in a frozen solution of CH_2Cl_2. Temperature dependence of the magnetization relaxation times (τ) in the absence of an applied field (e) and under a 800 Oe applied static field (f). The solid red lines represent the best fit of the data to Eq. 2 or 3. The blue, purple, and teal lines are the individual components of the relaxation model for the Orbach, Raman, and QTM processes.

Additional optical characterization

Optical properties of [Dy_2(bpm)(tfaa)$_6$] (1)

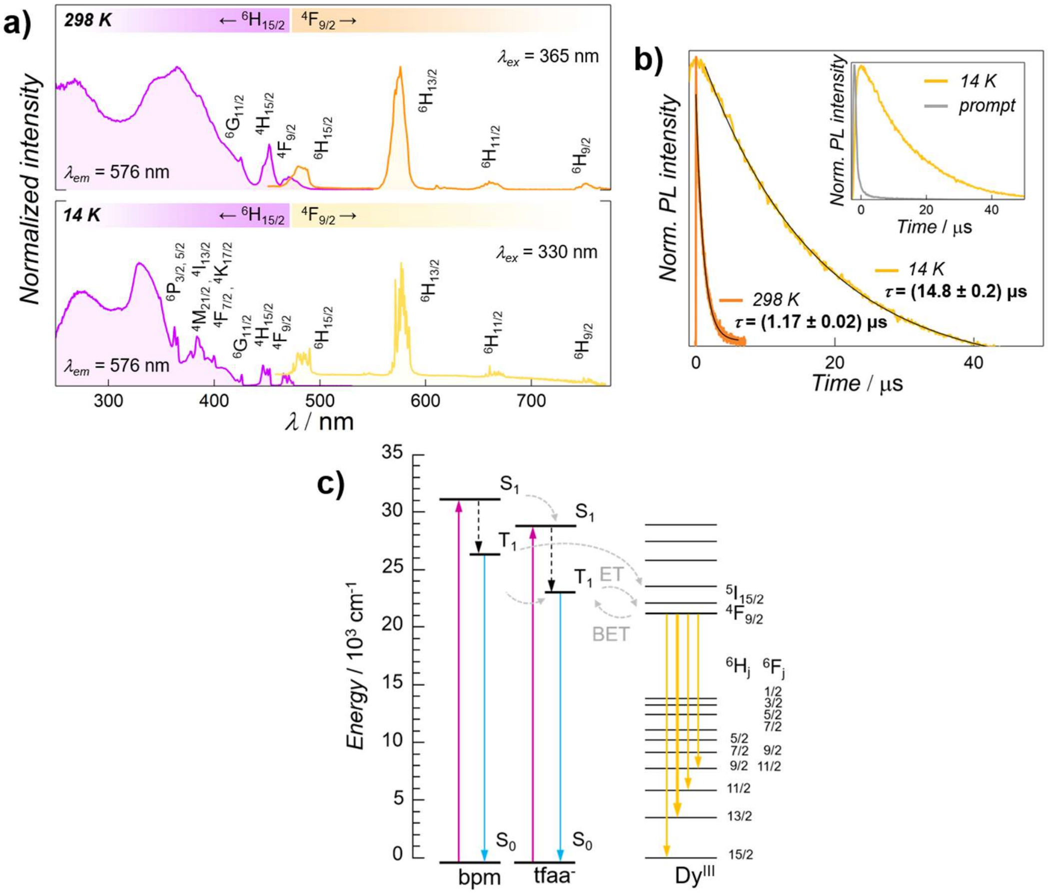

Figure S10. The photoluminescence (PL) properties of **1** were tested at room temperature (298 K) and 14 K (a). The excitation spectra (left) were obtained monitoring the emission in correspondence of the $^4F_{9/2} \rightarrow {}^6H_{13/2}$ transition of Dy^{III} (576 nm). They show broad features, arising from the ligands, along with narrow bands due to direct Dy^{III} excitation. The emission spectra (right) were recorded under UV excitation exploiting the ligand absorption followed by energy transfer (ET) to the lanthanide ion. At both temperatures, the typical visible emission bands of Dy^{III} characterize the emission of **1**. At 14 K, the Stark splitting of the electron levels becomes better appreciable, hence the emission bands are observed as well-resolved manifolds. The PL decay curves (b) were recorded monitoring the $^4F_{9/2} \rightarrow {}^6H_{13/2}$ transition of Dy^{III} (576 nm) exciting at 330 (14 K) and 340 nm (298 K). The decrease of the lifetime at room temperature, compared to 14 K, is induced by the $^4F_{9/2}$ level depopulation stemming from the thermal coupling of this Dy^{III} level with the $^5I_{15/2}$ level, along with the increased probability of back-ET (BET) to the ligands (c). The signal of the excitation lamp used for the PL decay measurements at 298 K is plotted in the inset in (b) along with the decay curve of **1**.

Optical properties of [Gd_2(bpm)(tfaa)$_6$] (2)

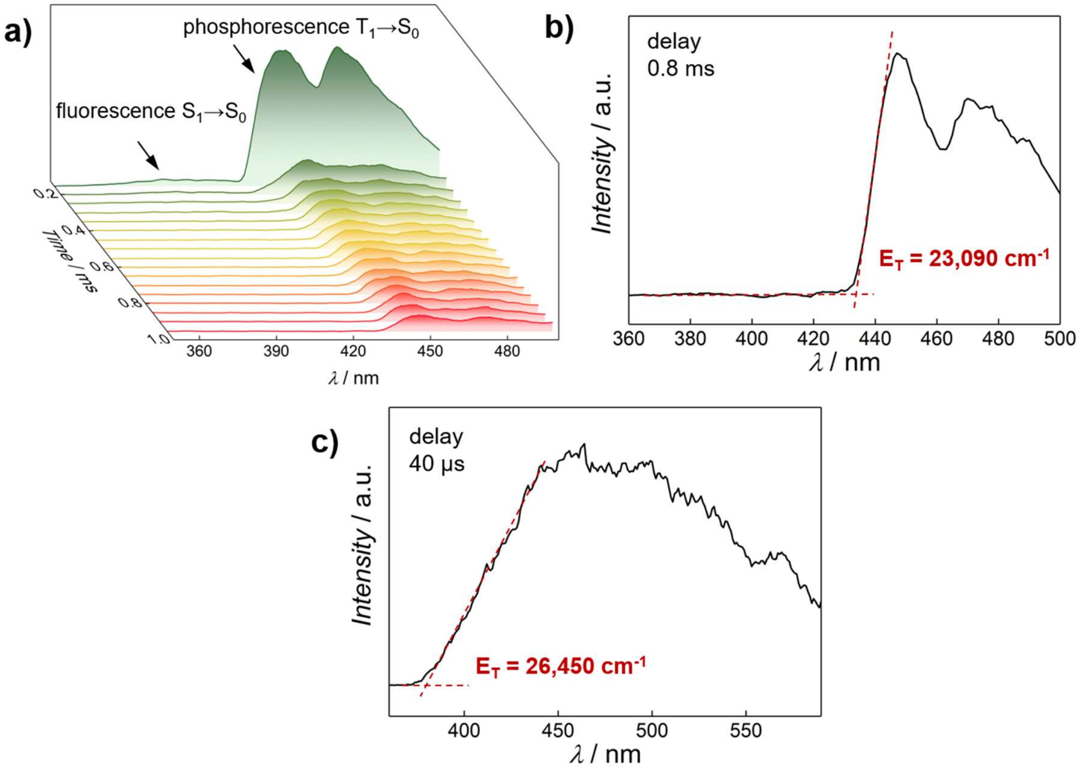

Figure S11. Time-resolved measurements were performed on the Gd^{III} analogue of **1** to separate the fluorescence ($S_1 \rightarrow S_0$) signal of the ligand scaffold from the phosphorescence ($T_1 \rightarrow S_0$) (a). The phosphorescence emission spectrum recorded 0.8 ms after the excitation of the complex was used to determine the position of the triplet state of the system (23090 cm^{-1})–corresponding to the triplet state of $tfaa^-$ (b). To determine the position of the triplet state of bpm, time-resolved solid-state studies were performed also on this ligand (c). The signal recorded with a delay of 40 μs from the excitation returns a value of 26450 cm^{-1}. The spectra were recorded under 330 nm excitation at 14 K.

High-resolution spectra of [Dy_2(bpm)(tfaa)$_6$] (1) recorded at 14 K

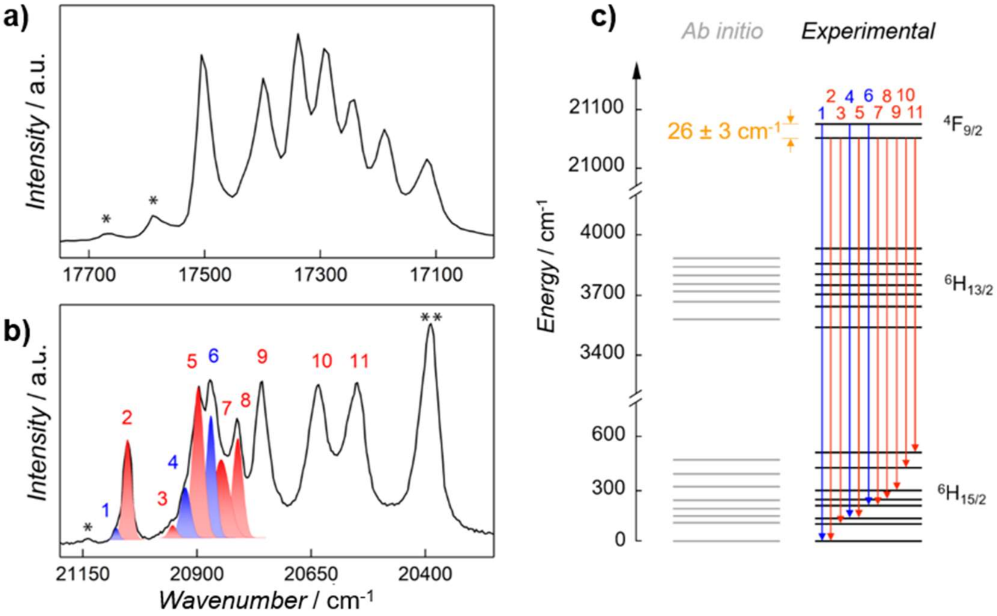

Figure S12. High-resolution spectra obtained under 365 nm excitation at 14 K for the $^4F_{9/2} \rightarrow {}^6H_{13/2}$ (a) and $^4F_{9/2} \rightarrow {}^6H_{15/2}$ (b) Dy^{III} transitions were used to build a partial energy level diagram (c). Considering the general form of the term symbol to describe an energy level ($^{2S+1}L_J$) and assuming only the first m_j state of $^4F_{9/2}$ populated, each manifold is expected to be composed of (J+1/2) components, as a consequence of the Stark splitting. This observation stems from the fact that Dy^{III} in **1** has an odd number of 4*f* electrons and occupies a low-symmetry environment (see crystallographic data, Table S1). However, additional signals are observed in both high-resolution spectra (noted with *), suggesting that not only the two lower m_j levels of the excited states are populated. The higher number of components observed for the $^4F_{9/2} \rightarrow {}^6H_{15/2}$ Dy^{III} transition made a deconvolution step necessary to separate the contributions coming from the second Stark sublevels of $^4F_{9/2}$. The color code and numbering used in b) were used in c) to mark the corresponding transitions, in order to make their assignation visually clear. From the deconvolution procedure, an energy difference of (26 ± 3) cm^{-1} was calculated between the first two Stark sublevels of $^4F_{9/2}$. From c), it is evident the good agreement between the position of the Stark sublevels of $^6H_{13/2}$ and $^6H_{15/2}$ Dy^{III} levels obtained from the experimental spectroscopic data and the *ab initio* calculations. The transition marked with ** in b) possibly stems from Tm^{III} impurities in the compound form the starting lanthanide source.

Comparison of the results from luminescence measurements and *ab initio* calculations

Table S6. Position of the Stark sublevels of the $^6H_{15/2}$ (upper table) and $^6H_{13/2}$ (lower table) Dy^{III} levels obtained from experimental luminescence data and *ab initio* calculations.

Kramers Doublet **$^6H_{15/2}$ Dy^{III} level**	***Luminescence*** **cm^{-1}**	***Calculations*** **cm^{-1}**
KD1	0	0
KD2	97	101.5
KD3	156	146.7
KD4	181	191.0
KD5	240	234.8
KD6	292	316.4
KD7	419	384.5
KD8	503	467.1

Kramers Doublet **$^6H_{13/2}$ Dy^{III} level**	***Luminescence*** **cm^{-1}**	***Calculations*** **cm^{-1}**
KD1	3544	3584.7
KD2	3651	3672.5
KD3	3711	3726.0
KD4	3756	3761.4
KD5	3808	3802.5
KD6	3860	3845.4
KD7	3934	3887.3

Luminescence intensity ratio (*LIR*) for the explored luminescence thermometry approaches

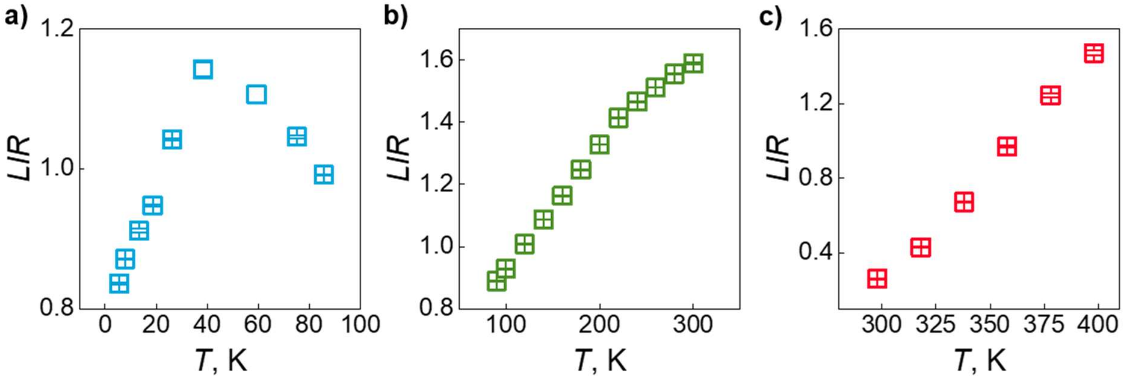

Figure S13. All the luminescence thermometry approaches proposed in this study are ratiometric, *i.e.* they are based on a thermal parameter, luminescence intensity ratio – *LIR* –, that is the ratio between the integrated intensity of two separate photoluminescence signals originating from the system. While for the double-band method (c) the two signals are distinct bands ascribed respectively to the ligands' phosphorescence ($T_1 \rightarrow S_0$) and $^4F_{9/2} \rightarrow {}^6H_{15/2}$ Dy^{III} emission, for the single-band approach (a and b) the ratiometric approach is achieved upon considering the ratio between the high (560-577 nm) and low (578-592 nm) energy side of the $^4F_{9/2} \rightarrow {}^6H_{13/2}$ Dy^{III} integrated emission. From the experimentally obtained *LIR* values, the numerical derivative was obtained and used to calculate the associated relative thermal sensitivity (S_r – see Eq. 6 in the main text, Methods). It is important to underscore that, due to practical constraints, the measurements below room temperature in the two different ranges were performed using different experimental conditions from the viewpoint of excitation wavelength (330 *vs.* 405 nm) and detection apparatus. Regarding the excitation source, at 405 nm the absorption of **1** shows a considerable contribution from the direct Dy^{III} absorption as opposed to 330 nm, where the ligand scaffold is mainly responsible for the light absorption (see Figure S10). Hence, the thermal response of the profile of $^4F_{9/2} \rightarrow {}^6H_{13/2}$ Dy^{III} emission under the two different excitation wavelengths is expected to differ. Moreover, although the optical response to thermal variations of a material is an intrinsic property, the performance as a luminescent thermometer also depends on the experimental setup utilized to assess it. Therefore, it would be of little significance to compare the absolute values observed for the luminescence intensity ratio (*LIR*) and the relative thermal sensitivity in the two cases.

Thermometry in a luminescent polymeric film of {Dy$_2$}

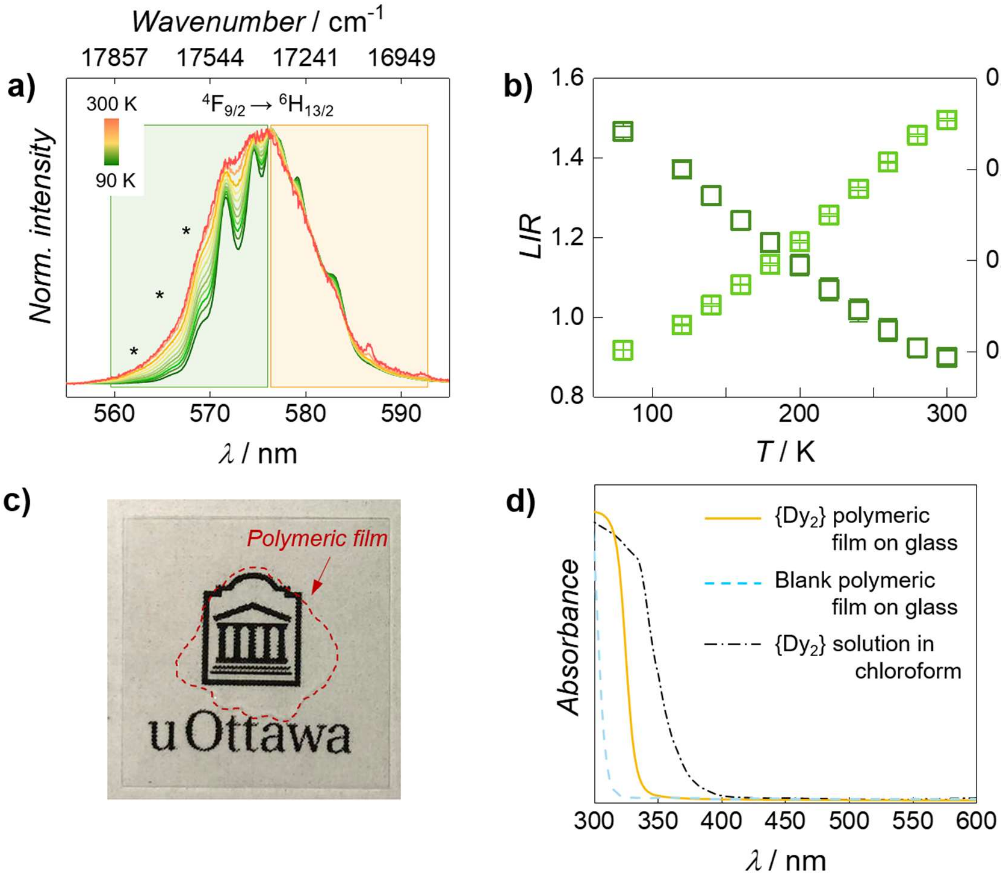

Figure S14. To prove the capability of the {Dy$_2$} dinuclear complex to act as a luminescent thermometer at a molecular level, we prepared a polymeric film mixing 200 μL of a 2 mg/mL chloroform solution of the complex with 350 μL of commercially available transparent nail polish. 10 μL of the mixture was casted on a copper holder and then the solvent was allowed to dry off overnight. The so-obtained transparent luminescent film was used to perform luminescence thermometry in the 80-300 K temperature range (a and b). $^4F_{9/2} \rightarrow {}^6H_{13/2}$ Dy^{III} emission profile shows a comparable thermal dependence observed for the compound in its crystalline form. The use of the ratiometric approach described in the main manuscript for the single-band thermometry returns a S_r ranging from 0.20 to 0.32 % K^{-1}. The discrepancy between the values obtained for the crystalline form (main text, Figure 3e) and for the luminescent polymeric film is to be ascribed to the different chemical environment experienced by the complex molecule either closely packed in a crystalline lattice or singly dispersed in a polymeric matrix, and the different phonon density in the two situations. The apparent transparency of the polymeric film (c - here prepared on a glass slide for a better visualization) suggests the absence of light scattering, as also confirmed by the optical absorption measurements performed of the same film (d). The absence of light scattering is a clear indication of the lack of large crystals formation upon evaporation of the solvent. In this situation of “frozen solution”, the molecules of the complex acts as independent entities, responding individually to optical stimuli. Therefore, the thermometric behavior observed originates at the single molecule level.

Thermometry cycles

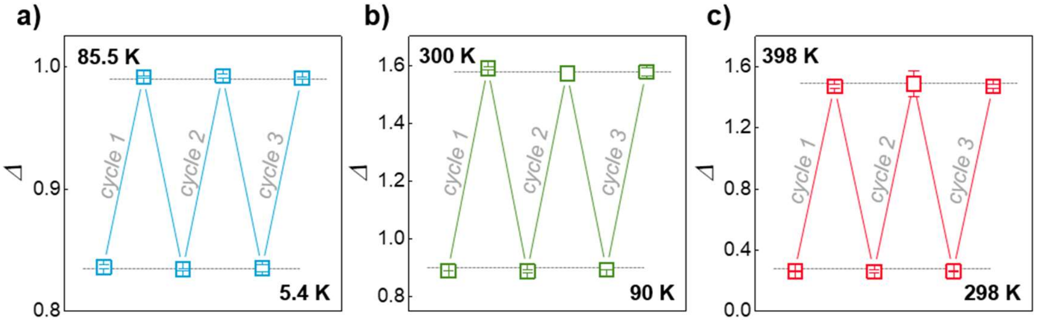

Figure S15. Repeatability study for the single-band (a and b) and double-band (c) luminescence thermometry approaches proposed in this study. Repeatability is calculated as $R = 1 - \max(|\Delta_i - \Delta_c|)/\Delta_c$, where Δ_i is the thermal parameter obtained at each measurement and Δ_c is the thermal parameter extracted from the calibration curve.[1] The associated repeatability of these approaches is a - 99.7 %, b - 98.9 % and c - 98.8 %, respectively.

---

[1] C. D. S. Brites, A. Millán, L. D. Carlos *Lanthanides in Luminescent Thermometry* in Handbook of the Physics and Chemistry of Rare Earths, **2016**, *vol. 49*, ch. 281, p. 367 Elsevier

“***Narrow-bands approach***”

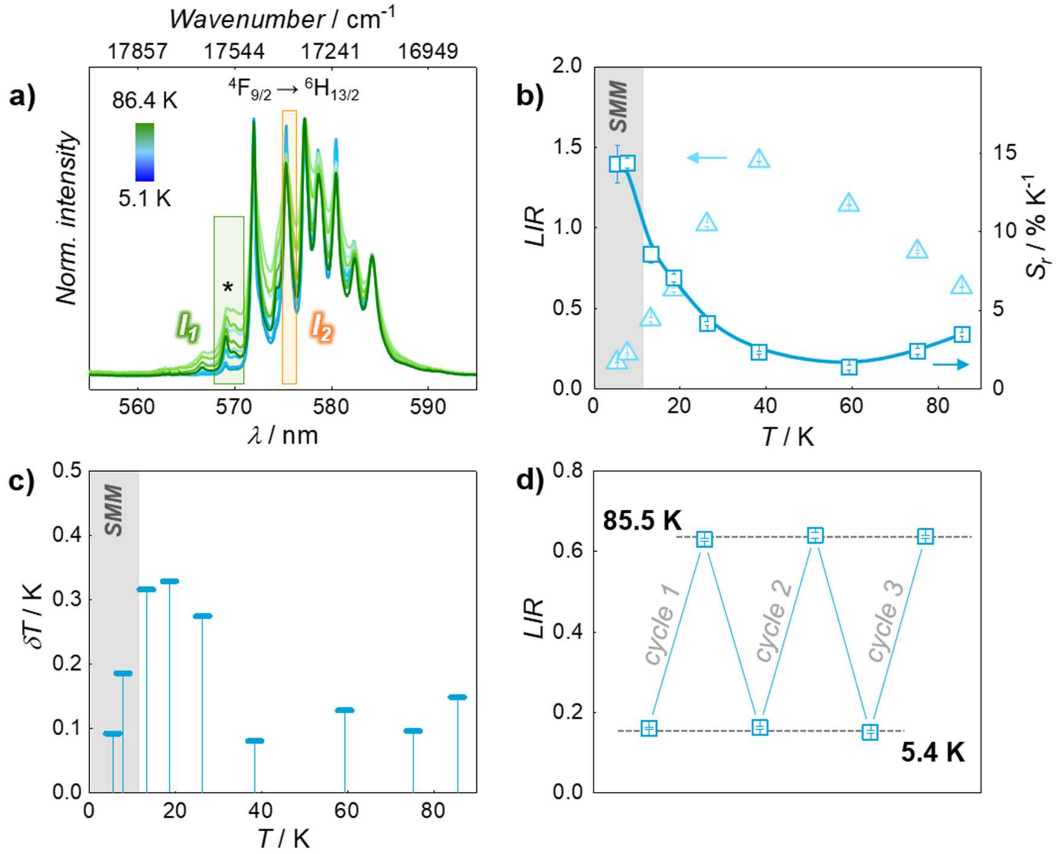

Figure S16. Temperature-dependent emission spectrum of **1** (Dy^{III} $^4F_{9/2} \rightarrow {}^6H_{13/2}$ transition) with highlighted integration ranges (shaded rectangles: green - I_1; orange - I_2) used in the alternative luminescent thermometry approach (a). These ranges encompass respectively the 0-1 emission line of the $^4F_{9/2} \rightarrow {}^6H_{13/2}$ transition (575.1-575.6 nm) and a so-called “hot-band” (marked with an asterisk) arising from the thermally induced population of high energy $^4F_{9/2}$ Stark sublevels (568.2-570.5 nm). Corresponding *LIR* and S_r values (b). Associated temperature uncertainty (c) and repeatability test (d).

Effect of magnetic fields on the luminescence of {Dy$_2$}

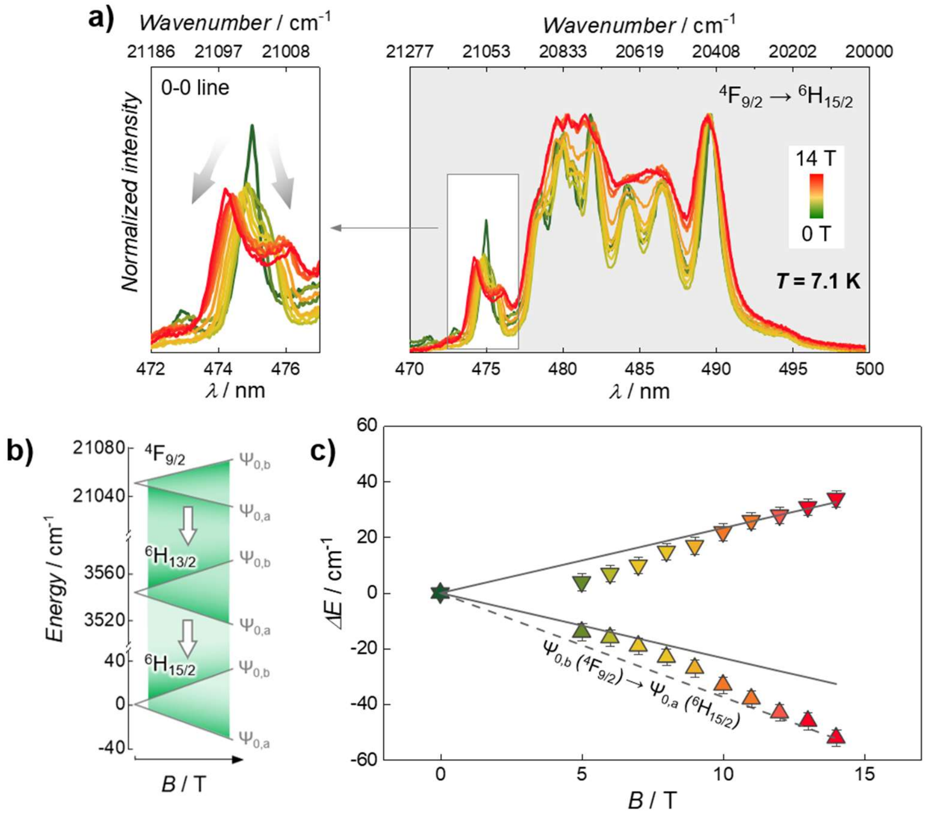

Figure S17. Zeeman effect on the emission $^4F_{9/2} \rightarrow {}^6H_{15/2}$ band of Dy^{III} varying the applied magnetic field at a fixed temperature of 7.1 K (a). The Zeeman splitting can be theoretically estimated using the expression in Eq. 4 reported in the main manuscript, obtaining the results reported in b). The 0-0 line of the multiplet (zoom-in in a) was considered to give a quantitative evaluation of the Zeeman splitting. The maxima of the two components in which the 0-0 line gets split at each temperature were identified (data points in c) and compared to the simulated trend of the Zeeman energy (solid grey lines in c). Deviation from the expected values could be rationalized considering transitions stemming from the highest level of the 9/2 m_j split doublet of $^4F_{9/2}$ (here $\Psi_{0,b}$ – dashed line). It is worth mentioning that this deviation is consistent with the one observed for the $^4F_{9/2} \rightarrow {}^6H_{13/2}$ band (see Figure 4c in the main manuscript).

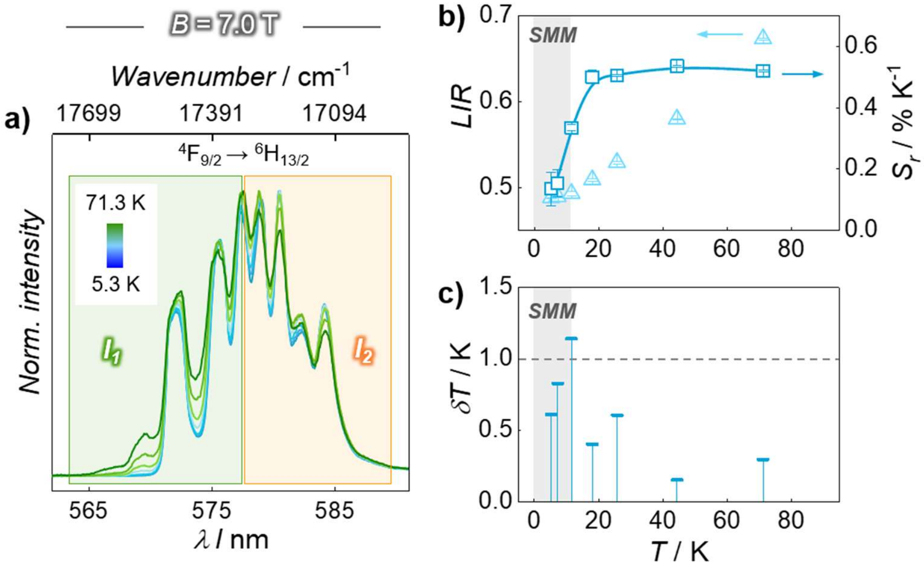

Figure S18. Single-band thermometry approach applied under an applied magnetic field *B* = 7 T. The spectral profile and the temperature-dependent variations (a) are considerably different from the ones observed under no or weak (0.8 T) magnetic field (see Figure 3 and 4 in the main manuscript). The *LIR* obtained from the ratio of the areas indicated by the shaded rectangles (green – I_1; orange – I_2) increases much less steeply than in the previously discussed cases (no or 0.8 T field) and the resulting S_r is lower (b). Note that S_r is minimum in the temperature range of interest (SMM), where the uncertainty is always above 1 K (c).